ARTICLE   OPEN

Check for updates

Cigarette smoke causes a bioenergetic crisis in RPE cells involving the downregulation of HIF-1α under normoxia

Yoshiyuki Henning [1✉], Katrin Willbrand[1], Safa Larafa [2], Gesa Weißenberg[1], Veronika Matschke[3], Carsten Theiss[3], Gina-Eva Görtz[4,5] and Johann Matschke [2,5]

Age-related macular degeneration (AMD) is the most common blinding disease in the elderly population. However, there are still many uncertainties regarding the pathophysiology at the molecular level. Currently, impaired energy metabolism in retinal pigment epithelium (RPE) cells is discussed as one major hallmark of early AMD pathophysiology. Hypoxia-inducible factors (HIFs) are important modulators of mitochondrial function. Moreover, smoking is the most important modifiable risk factor for AMD and is known to impair mitochondrial integrity. Therefore, our aim was to establish a cell-based assay that enables us to investigate how smoking affects mitochondrial function in conjunction with HIF signaling in RPE cells. For this purpose, we treated a human RPE cell line with cigarette smoke extract (CSE) under normoxia (21% O_2), hypoxia (1% O_2), or by co-treatment with Roxadustat, a clinically approved HIF stabilizer. CSE treatment impaired mitochondrial integrity, involving increased mitochondrial reactive oxygen species, disruption of mitochondrial membrane potential, and altered mitochondrial morphology. Treatment effects on cell metabolism were analyzed using a Seahorse Bioanalyzer. Mitochondrial respiration and ATP production were impaired in CSE-treated cells under normoxia. Surprisingly, CSE-treated RPE cells also exhibited decreased glycolytic rate under normoxia, causing a bioenergetic crisis, because two major metabolic pathways that provide ATP were impaired by CSE. Downregulation of glycolytic rate was HIF-dependent because HIF-1α, the α-subunit of HIF-1, was downregulated by CSE on the protein level, especially under normoxia. Moreover, hypoxia incubation and treatment with Roxadustat restored glycolytic flux. Taken together, our in vitro model provides interesting insights into HIF-dependent regulation of glycolysis under normoxic conditions, which will enable us to investigate signaling pathways involved in RPE metabolism in health and disease.

INTRODUCTION

Retinal pigment epithelium (RPE) cells, a monolayer of pigmented cells located adjacent to the photoreceptors, serve as a gatekeeper, which regulates the transport of nutrients, oxygen, and ions from the choriocapillaris to the photoreceptors as well as the disposal of metabolic end-products [1]. In addition, RPE cells protect photoreceptors from light-induced damage, support the renewal of photoreceptor outer segments by phagocytosis, and execute the visual cycle, to mention a few functions [1]. Furthermore, there is a fine-tuned metabolic interaction of RPE cells and photoreceptors. RPE cells, which mainly produce ATP by mitochondrial respiration, supply glucose to the photoreceptors. Photoreceptors, in turn, generate energy mainly by aerobic glycolysis and supply the RPE cells with the resulting lactate to fuel mitochondrial respiration [2, 3]. Consequently, dysregulation of the photoreceptor–RPE interaction results in visual disorders, such as age-related macular degeneration (AMD). AMD is the most common blinding disease in industrial countries diagnosed in people of 60 years and older. Globally, it represents the third leading cause of irreversible vision loss worldwide with increasing

prevalence [4–6]. In the later stages of AMD, about 90% of the patients develop dry AMD or geographic atrophy, which is associated with dysfunction and gradual degeneration of RPE cells, choriocapillaris, and photoreceptors. There is still no convincing treatment for dry AMD due to a lack of mechanistic understanding driving the disease [7]. Thus, to develop novel treatment options, a deeper understanding of early AMD pathophysiology and its risk factors is necessary.

Major hallmarks often observed in early AMD are thickening of the Bruch's membrane, reduced choroidal blood flow, and the appearance of drusen, deposits of metabolic products accumulating between the RPE and Bruch's membrane [6, 8–10]. These structural changes impair the oxygen supply of the RPE and photoreceptors, resulting in hypoxia, a state where oxygen demand exceeds the supply. Hypoxia results in the stabilization of hypoxia-inducible factors (HIFs), which regulate the adaptation to hypoxic conditions by, e.g. initiating a metabolic switch from oxidative phosphorylation (OXPHOS) to glycolysis or expression of proangiogenic growth factors. HIFs are dimeric transcription factors with an oxygen-labile α-subunit and a constitutively

2

expressed β-subunit located in the nucleus [11, 12]. When oxygen is available at physiological levels, α-subunits are constantly degraded after hydroxylation by oxygen-dependent prolyl hydroxylases 1–3 (PHD1, PHD2, and PHD3) [13]. To date three HIF isoforms are known from which HIF-1 and HIF-2 are considered most relevant for the hypoxia response [14]. HIFs are protective in the short-term, but chronic HIF stabilization in the RPE can exert detrimental effects [15–18], from which the metabolic shift is most relevant for the present study. Interestingly, there is increasing evidence from different models, including human AMD donor cells, that dysregulation of RPE energy metabolism contributes to AMD pathophysiology [19–25]. Accordingly, improvement of mitochondrial function has been proposed as an early intervention strategy against dry AMD [26, 27].

The many risk factors contributing to the development of AMD are divided into non-modifiable and modifiable risk factors. While the age of a person is the most important non-modifiable risk factor, smoking is the most important modifiable risk factor [9]. Cigarette smoke or cigarette smoke extract (CSE), which is used in cell culture experiments, promotes several pathophysiological processes associated with AMD in RPE and surrounding tissues, including oxidative stress, inflammation, cell senescence, and neovascularization resulting in a significantly increased risk to develop AMD [4, 6, 9, 28]. Furthermore, CSE has adverse effects on mitochondrial integrity in RPE cells [29–31] as well as lung, airway, and bronchial epithelial cells [32–36]. Moreover, in cultured fibroblasts, CSE enhanced HIF-1α stabilization and HIF signaling [37]. Therefore, we hypothesized that CSE-induced impairment of mitochondrial function is regulated in a HIF-dependent manner and that targeting HIF might represent an interventional strategy against mitochondrial dysfunction. For this purpose, we developed a cell-based assay that enabled us to conduct a detailed characterization of energy metabolism and mitochondrial integrity of CSE-treated RPE cells and analyzed the involvement of HIF signaling in the metabolic phenotype of these cells.

RESULTS
CSE-treated cells displayed reduced mitochondrial respiration and glycolytic capacity
In order to investigate how CSE affects mitochondrial function, we analyzed oxidative phosphorylation (OXPHOS) by using a Seahorse XFe96 Analyzer (Fig. 1A). In particular, we determined basal respiration, mitochondrial ATP production, and maximal respiration (Fig. 1B) under normoxic conditions (21% O_2) after cells were treated with CSE for 16 h. All parameters were decreased by CSE-treatment in a concentration-dependent manner. In the next step, we analyzed glycolysis, which usually compensates for reduced mitochondrial ATP production by OXPHOS (Fig. 1C). However, both, basal glycolysis as well as compensatory glycolysis were decreased by CSE in a concentration-dependent manner (Fig. 1D). Next, we measured α-ketoglutarate concentrations, an intermediate of the tricarboxylic acid (TCA) cycle. We found that α-ketoglutarate concentrations in ARPE-19 cells treated with 5% CSE were significantly higher compared to controls (Fig. 1E). To exclude the possibility that treatment with 5% CSE impairs cell viability, leading to the observed effects, we measured LDH release, which was not affected by CSE treatment up to a CSE concentration of 15% (Fig. 1F). Taken together, overall ATP production by mitochondrial respiration and glycolysis was impaired by CSE treatment.

CSE treatment reduced HIF-1α protein levels via differential mechanisms depending on oxygen levels
HIFs are one of the main regulators of glycolysis-driven ATP production. Therefore, we measured HIF protein levels in ARPE-19 cells treated with 5% CSE in a time-course experiment in hypoxia and normoxia. We observed significantly decreased HIF-1α protein

levels after 4 and 8 h of CSE treatment under hypoxia (1% O_2) (Fig. 2A). Furthermore, we measured hydroxylated HIF-1α levels under the same conditions as a measure of hydroxylation by PHDs and subsequent degradation, which was significantly upregulated after 4 h (Fig. 2B). In contrast, HIF-2α protein levels remained unchanged under hypoxic conditions (Fig. 2C). Under normoxic conditions (21% O_2), HIF-1α levels were significantly downregulated by 5% CSE after 18 h (Fig. 2D). HIF-2α showed a trend towards downregulation by CSE but the effect was not as pronounced as for HIF-1α (Fig. 2D). In addition, PHD inhibition by Roxadustat served as a positive control for HIF bands under normoxia (Fig. 2D). In contrast to hypoxic conditions, hydroxylated HIF-1α levels were significantly lower in cell treated with 5% CSE (Fig. 2E). HIF1A and HIF2A mRNA expression was not affected by CSE (Fig. 2F). To test downstream effects of HIF-1α destabilization, we measured gene expression of the Carbonic Anhydrase 9 (CA9), a specific target gene of HIF-1. CA9 expression was downregulated by CSE treatment under normoxia but not hypoxia (Fig. 2G).

CSE treatment impaired mitochondrial integrity
We treated ARPE-19 cells with CSE and measured mitochondrial reactive oxygen species (ROS) by flow cytometry. Mitochondrial ROS was significantly increased in CSE-treated cells after treatment with 5% CSE for 16 h under normoxia (Fig. 3A). Furthermore, we measured mitochondrial membrane potential in TMRE-stained cells by flow cytometry as a measure of mitochondrial membrane integrity. Compared to controls, mitochondrial membrane potential was upregulated (hyperpolarized) after treatment with 5% CSE for 16 h (Fig. 3B). In addition, we stained the cells with MitoTracker Deep Red, a polarization-dependent fluorescence staining of mitochondria [38, 39]. In cells treated with 5% CSE for 8 h, we found fainter and less pronounced staining of mitochondria, which confirmed mitochondrial depolarization detected by flow cytometry (Fig. 3C). For detailed examination of mitochondrial morphology in CSE-treated ARPE-19 cells, we conducted TEM analyses (Fig. 3D). Compared to controls, cells treated with 5% CSE displayed larger (Fig. 3E, F) and elongated (Fig. 3G–J) mitochondria compared to the respective non-treated controls. Mitochondrial mass, assessed by Western blot analysis of TOM20 and HSP60, was not significantly changed by CSE treatment (Fig. 3K).

Hypoxia incubation and Roxadustat treatment restored glycolytic capacity
To determine whether metabolic reprogramming induced by CSE treatment and resulting HIF destabilization are related, we tested whether the glycolytic rate is restored after stabilization of HIF protein by hypoxia or Roxadustat. In the first approach, we treated ARPE-19 cells with 3% and 5% CSE for 6 h under normoxia and hypoxia (1% O_2). The hypoxia group was additionally pre-incubated at 1% O_2 for 2 h prior to CSE treatment (Fig. 4A, B). In a second approach, we treated ARPE-19 cells with CSE for 12 h under normoxia and hypoxia without pre-incubation (Fig. 4C, D). Both approaches significantly downregulated basal and compensatory glycolysis of CSE-treated cells under normoxia as observed in previous experiments. However, hypoxic treatment for either 6 or 12 h fully restored basal and compensatory glycolysis of CSE-treated ARPE-19 cells to the levels observed under normoxic conditions in non-treated cells (6 h: Fig. 4B; 12 h: Fig. 4D). Next, ARPE-19 cells were treated with Roxadustat, a specific PHD inhibitor, which stabilizes HIF-1α and HIF-2α in a concentration-dependent manner (Fig. 4E). Co-treatment with CSE and Roxadustat for 16 h significantly upregulated basal and compensatory glycolysis compared to CSE treatment alone (Fig. 4F, G), clearly indicating that CSE treatment impairs glycolytic capacity by fostering PHD-induced HIF degradation. As
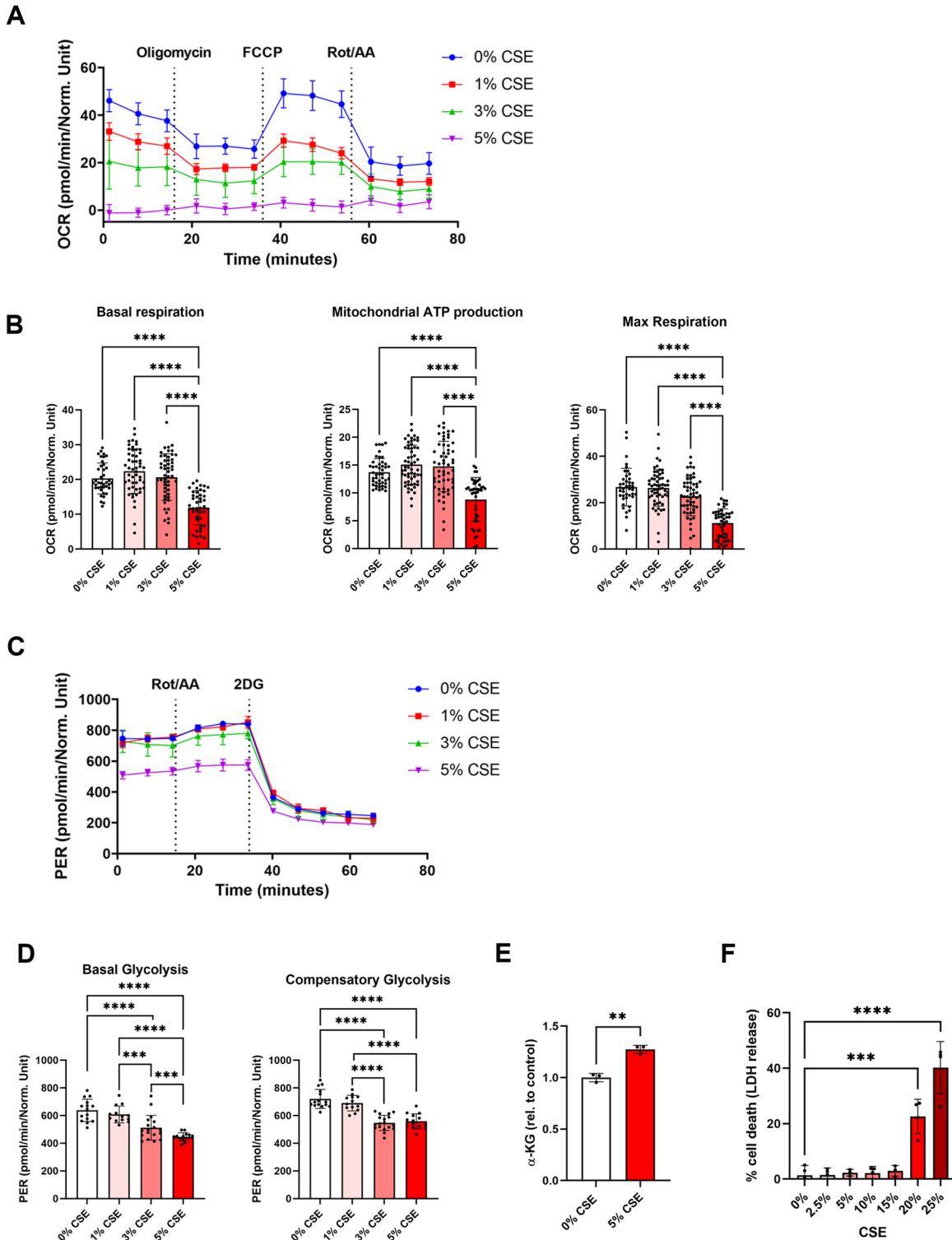
Fig. 1 Mitochondrial respiration and glycolytic flux in CSE-treated ARPE-19 cells. A Mitochondrial oxygen consumption rate (OCR) representing oxidative phosphorylation in ARPE-19 cells treated with different CSE concentrations was determined by using a Mitochondrial Stress Test and a Seahorse XFe96 Analyzer. **B** Basal respiration, mitochondrial ATP production, and maximum respiration of CSE-treated ARPE-19 cells based on a Mitochondrial Stress Test. Data was obtained from $n = 4–8$ wells for each independent sample ($N = 6–8$ per treatment group). **C** Proton efflux rate (PER) representing glycolytic rate in ARPE-19 cells treated with different CSE concentrations determined with a Glycolysis Rate Assay using a Seahorse XFe96 Analyzer. **D** Basal and compensatory glycolysis of CSE-treated ARPE-19 cells based on a Glycolysis Stress Test. Data was obtained from $n = 4–8$ wells for each independent sample ($N = 3$ per treatment group). **E** Measurement of α-ketoglutarate (α-KG) in CSE-treated cells expressed relative to untreated control cells ($N = 3$). **F** LDH release as a measure of cell death from cells treated with different CSE concentrations. Seahorse and LDH datasets were statistically analyzed with one-way ANOVA followed by Tukey's multiple comparisons test and α-ketoglutarate measurement was analyzed with unpaired t-test. $**p < 0.01$, $***p < 0.001$, and $****p < 0.0001$.
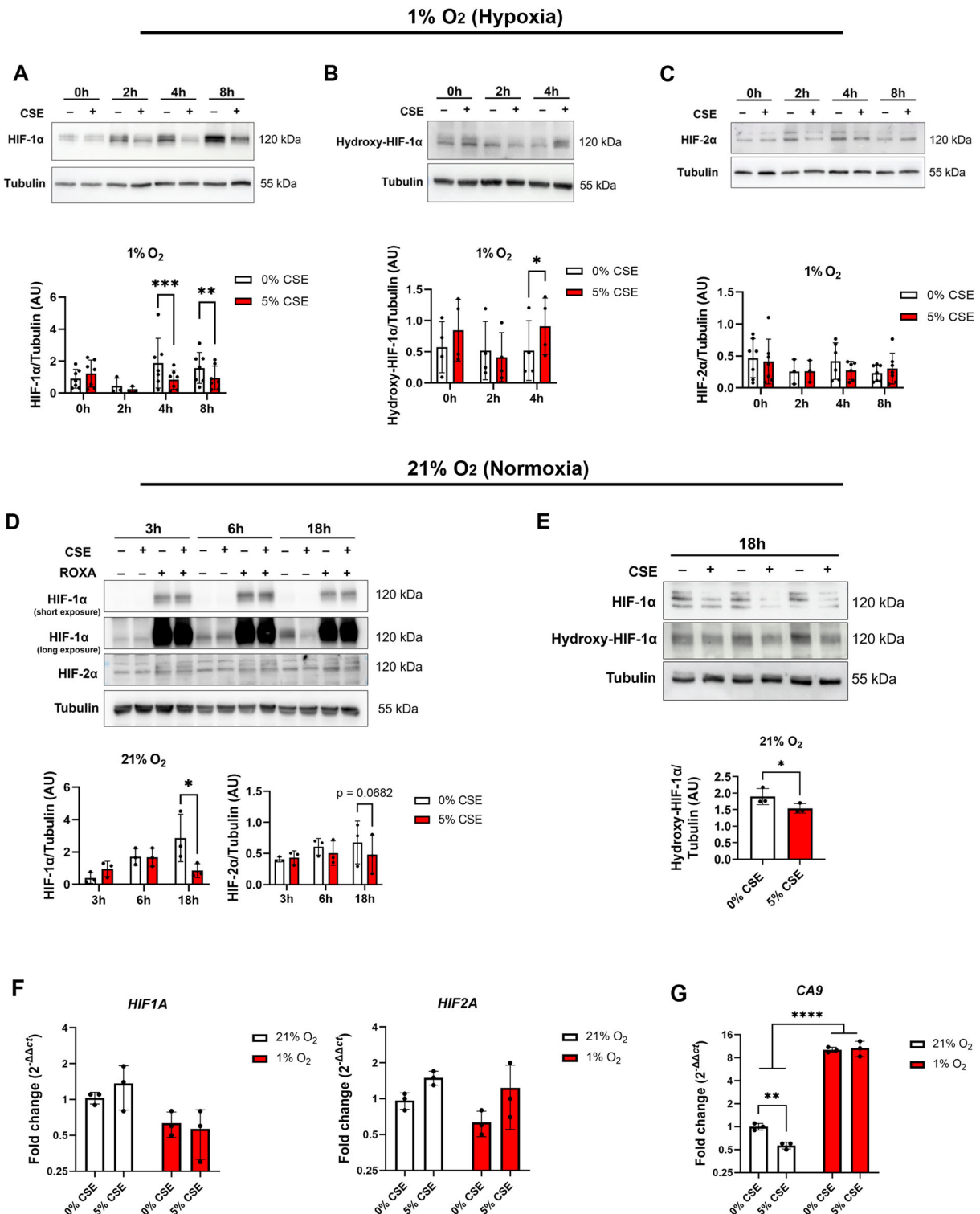
Fig. 2 Quantification of HIF protein and mRNA expression levels under normoxic and hypoxic conditions. Representative images and statistical analyses of **A** HIF-1α, **B** hydroxy-HIF-1α, and **C** HIF-2α protein levels normalized to α-Tubulin in ARPE-19 cells treated with 5% CSE at 1% O_2 compared to controls assessed at different timepoints ($N = 3$–7). **D** Representative images and statistical analyses of HIF-1α and HIF-2α protein levels normalized to α-Tubulin in ARPE-19 cells treated with 5% CSE compared to controls assessed at different timepoints at 21% O_2 with or without 30 μM Roxadustat (ROXA) as positive control. To depict HIF-1α bands in cells treated with ROXA, a short exposure time was chosen (<5 s). To depict HIF-1α bands in cells treated at 21% O_2 without ROXA, a long exposure time (>2 min) was chosen because HIF-1α is rapidly degraded under normoxia. **E** Representative images and statistical analyses of hydroxy-HIF-1α protein levels normalized to α-Tubulin in ARPE-19 cells from three independent groups treated with 5% CSE for 18 h at 21% O_2. HIF-1α is shown above to show downregulation of HIF-1α by CSE ($N = 3$). **F** Gene expression of *HIF1A* (left panel), *HIF2A* (right panel), and **G** *Carbonic Anhydrase 9* (*CA9*) in CSE-treated ARPE-19 cells under normoxia and hypoxia determined by qRT-PCR expressed as $2^{-\Delta\Delta ct}$ ($N = 3$). Western blot data were statistically analyzed with two-way ANOVA followed by Šídák's multiple comparisons test and qRT-PCR data were analyzed by two-way ANOVA followed by Tukey's multiple comparisons test. AU arbitrary units. *$p < 0.05$, **$p < 0.01$, ***$p < 0.001$, and ****$p < 0.0001$.
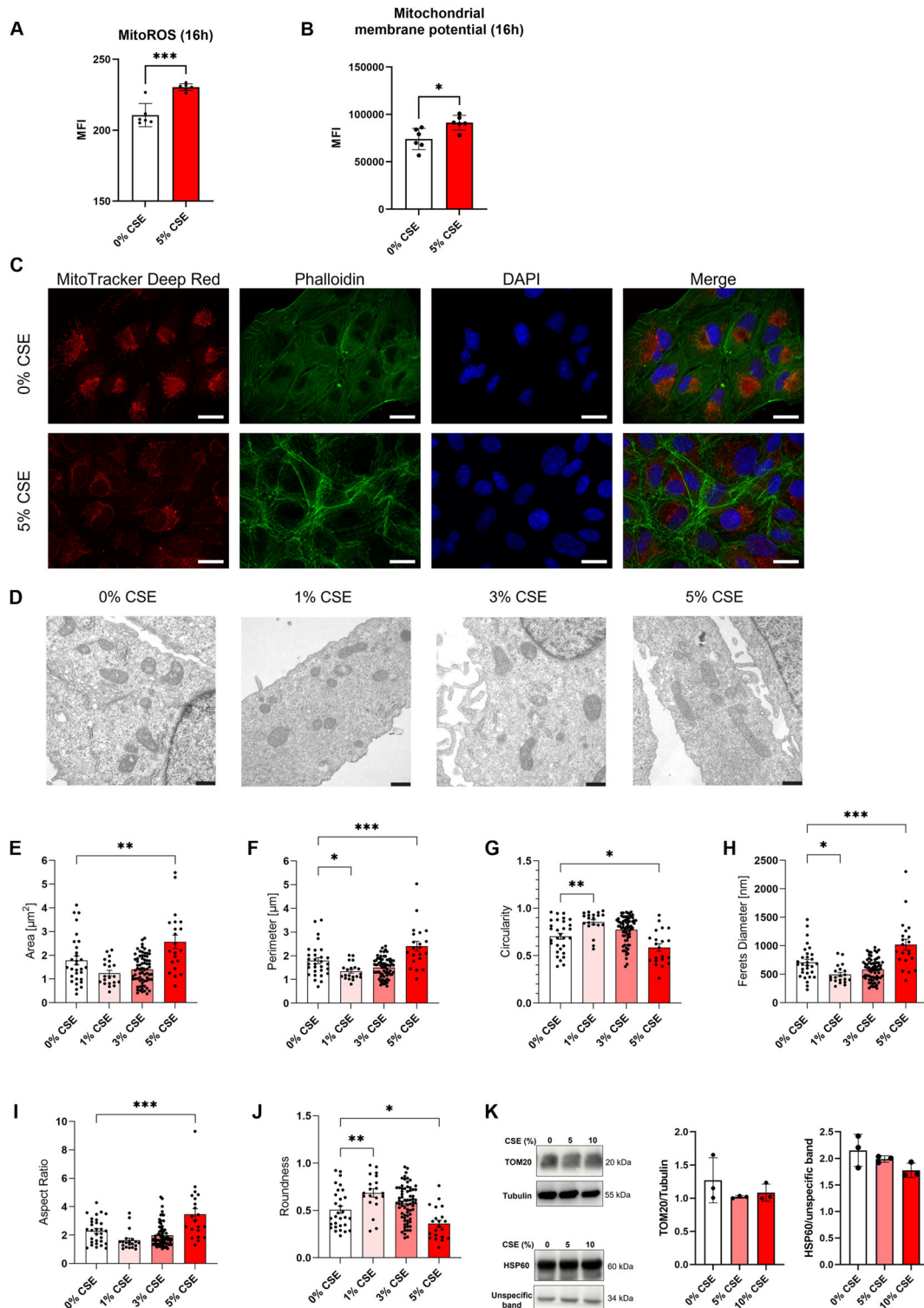
Fig. 3 Analysis of mitochondrial integrity of CSE-treated ARPE-19 cells. A Mitochondrial ROS (MitoROS) and **B** mitochondrial membrane potential in ARPE-19 cells treated with 5% CSE for 16 h compared to untreated controls determined by flow cytometry and expressed as mean fluorescence intensity (MFI; $N = 6$). **C** Staining of ARPE-19 cells treated with 5% CSE for 8 h compared to untreated controls with MitoTracker Deep Red, a polarization-dependent dye to visualize mitochondrial membrane potential. Cells were counterstained with Phalloidin and DAPI. Scale bar 20 μm. **D** TEM micrographs of ARPE-19 cells treated with different CSE concentrations. **E**, **F** Mitochondrial area and perimeter of mitochondria from cells treated with different CSE concentrations as a measure of mitochondrial size (20–70 mitochondria of one independent sample per treatment group). **G**–**J** Circularity, ferrets diameter, aspect ratio, and roundness of mitochondria from cells treated with different CSE concentrations as a measure of mitochondrial shape (20–70 mitochondria of one independent sample per treatment group). **K** Western blot quantification of TOM20 and HSP60 protein levels as a measure of mitochondrial mass ($N = 3$). Flow cytometry data were statistically analyzed with two-way ANOVA followed by Šídák's multiple comparisons test. TEM and Western Blot data were analyzed by one-way ANOVA followed by Tukey's or Dunnett's multiple comparisons test. *$p < 0.05$, **$p < 0.01$, ***$p < 0.001$, and ****$p < 0.0001$.
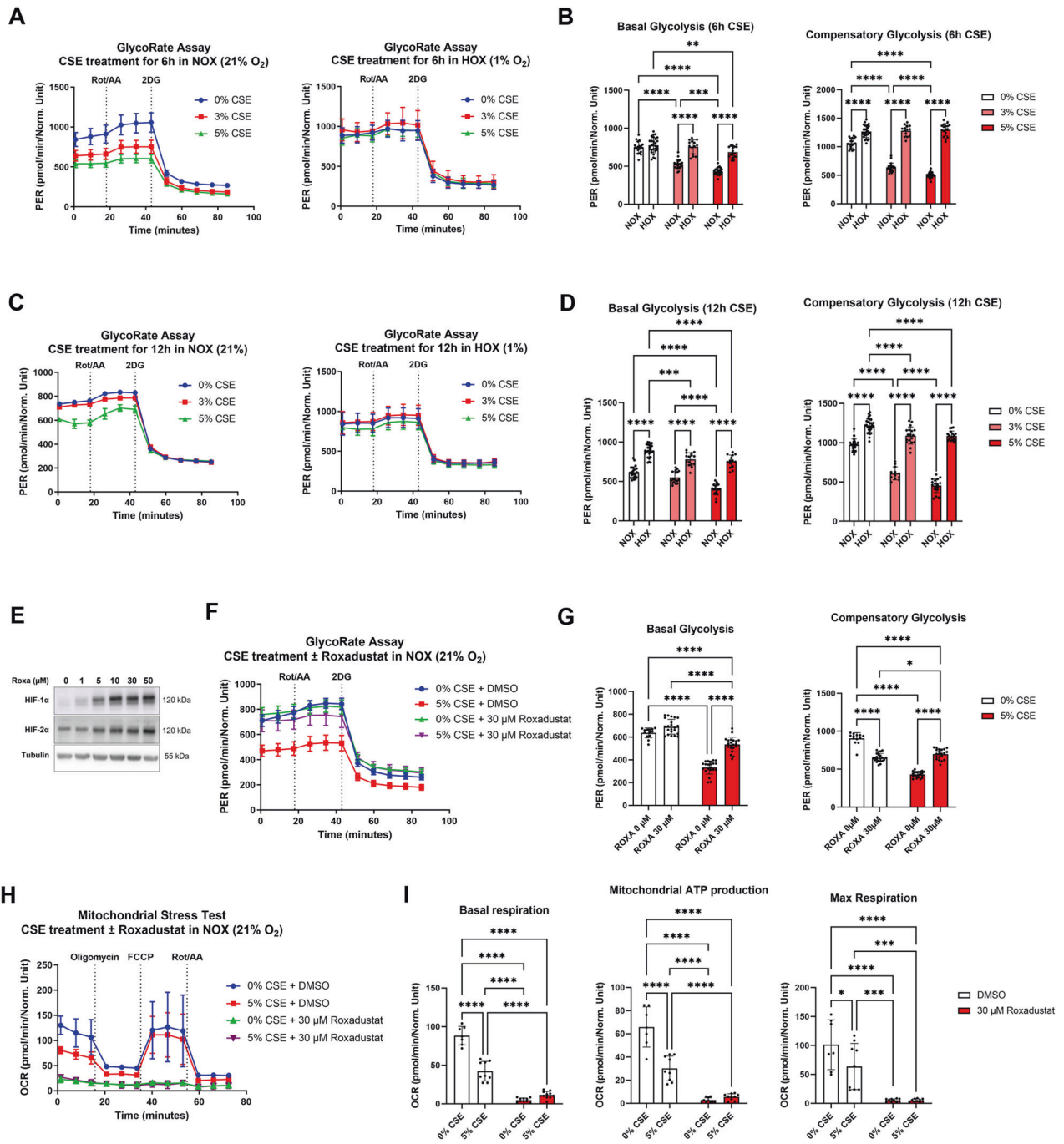
Fig. 4 Restoration of glycolytic flux in CSE-treated ARPE-19 cells by hypoxia or Roxadustat treatments. A Proton efflux rate (PER) representing glycolysis rate in ARPE-19 cells treated with different CSE concentrations determined with a Glycolysis Rate Assay using a Seahorse XFe96 Analyzer. Cells were treated for 6 h with 5% CSE under 21% and 1% O_2 with a 2 h preincubation under 21% or 1% O_2 prior to CSE treatment. **B** Basal and compensatory glycolysis of CSE-treated ARPE-19 cells based on a Glycolysis Stress Test. Data was obtained from $n = 4–13$ wells for each independent sample ($N = 3$ per treatment group). **C** PER of ARPE-19 cells treated with different CSE concentrations. Cells were treated for 12 h with 5% CSE under 21% and 1% O_2. **D** Basal and compensatory glycolysis of CSE-treated ARPE-19 cells. Data was obtained from ($N = 4–11$ wells for each independent sample ($N = 3$ per treatment group). **E** Stabilization of HIF-1α and HIF-2α in ARPE-19 cells treated with different Roxadustat concentrations for 6 h ($N = 3$). **F** PER of ARPE-19 cells treated with 5% CSE and/or 30 μM Roxadustat. **G** Basal and compensatory glycolysis of ARPE-19 cells treated with 5% CSE with or without 30 μM Roxadustat (ROXA). Data was obtained from $n = 2–8$ wells for each independent sample ($N = 3$ per treatment group). **H** OCR of ARPE-19 cells treated with 5% CSE with or without 30 μM Roxadustat. **I** Basal respiration, mitochondrial ATP production, and maximum respiration of CSE/Roxadustat-treated ARPE-19 cells. Data was obtained from $n = 7–11$ wells for each independent sample ($N = 3$ per treatment group). Datasets were analyzed with two-way ANOVA followed by Tukey's multiple comparisons test. *$p < 0.05$, **$p < 0.01$, ***$p < 0.001$, and ****$p < 0.0001$.

expected, OXPHOS was almost completely shut down by HIF stabilization using Roxadustat (Fig. 4H, I).

DISCUSSION

In the present study, we aimed to establish a cell-based assay that enables us to identify potential CSE effects and signaling pathways in RPE cells associated with metabolic dysregulation. We found that CSE treatment of ARPE-19 cells under normoxia resulted in downregulated basal respiration, mitochondrial ATP production, and maximum respiration, indicating impaired mitochondrial function. Usually, mitochondrial dysfunction results in increased glycolytic flux to prevent depletion of ATP [40–42]. Surprisingly, in CSE-treated ARPE-19 cells, we even observed a decreased glycolytic flux. Under physiological conditions, the HIF pathway tightly balances energy metabolism according to oxygen availability and other metabolic demands and as such it is one important regulator of the metabolic switch between mitochondrial respiration and glycolysis [43, 44]. However, despite downregulated OXPHOS, we found that HIF-1α protein levels were decreased in CSE-treated cells under normoxic and hypoxic conditions. Under normoxic conditions, CSE treatment led to the downregulation of *CA9*, a gene specifically targeted by HIF-1. This implies that the impact of CSE on HIF-1α is more evident under normoxic conditions, as the significant stabilization of HIF-1α in hypoxic conditions (due to O_2-dependent inhibition of PHDs) could obscure the effect of CSE. This is further supported by the restoration of glycolytic flux under hypoxic conditions in a HIF-1-dependent manner. It might be surprising that the downregulation of HIF-1α under normoxic conditions had downstream effects on target gene expression and glycolysis in the present study because HIF-1 is usually considered a hypoxia-regulated transcription factor. However, it has been reported that HIF-1 regulates glycolysis also under normoxic conditions in several cell types [45–47]. The present study supports these findings as glycolysis in ARPE-19 cells was also shown to depend on HIF-1 signaling under normoxic conditions. Downregulation of HIF-1α is in good agreement with the lack of upregulation of glycolysis in our study but is in contrast to HIF-1α regulation reported in orbital fibroblasts, where HIF-1α protein levels and HIF signaling were both upregulated by CSE treatment [37]. In contrast, no significant CSE effects on HIF-2α were observed in our study. Downregulation of HIF-1α in CSE-treated ARPE-19 cells is likely to be caused at the posttranslational level since we found no changes in *HIF1A* mRNA expression. Interestingly, while downregulation of HIF-1α under hypoxia was accompanied by higher levels of hydroxylated HIF-1α, HIF-1α hydroxylation was even downregulated by CSE under normoxic conditions. We can infer from these data, that hydroxylation by PHDs is not involved in CSE-induced downregulation of HIF-1α under normoxia.

CSE treatment increased intracellular α-ketoglutarate concentrations, indicating inhibition of α-ketoglutarate dehydrogenase multienzyme complex (KGDHC), the rate-limiting enzyme complex of the TCA cycle [48]. This may be due to increased mitochondrial ROS levels observed in ARPE-19 cells, which were described to reduce KGDHC activity resulting in α-ketoglutarate accumulation [49]. Hydroxylation of HIF proline residues by PHDs requires α-ketoglutarate as a co-substrate [50]. Moreover, it has been shown that increased α-ketoglutarate levels promote PHD activity in various cell types, including RPE cells [51]. Thus, accumulation of α-ketoglutarate upon CSE treatment might lead to enhanced PHD activation resulting in increased HIF-degradation at least under hypoxia, where hydroxylated HIF-1α was increased by CSE. Interestingly, it has been shown that PHD2 has a higher affinity for α-ketoglutarate and HIF-1α compared to PHD3, which preferentially (but not exclusively) hydroxylates HIF-2α [52, 53]. This could explain why HIF-2α protein levels remained mostly unchanged upon CSE treatment, while HIF-1α protein levels

significantly decreased in CSE-treated cells. On the other hand, decreased production of TCA cycle metabolites such as succinate and fumarate as a result of KGDHC inhibition by CSE treatment might reduce the transcriptional activity of HIFs also under normoxia [44, 54, 55].

Impairment of the electron transport chain (ETC) is one possible mechanism for increased mitochondrial ROS production via reverse electron transport to ETC complex 1 [56, 57], which could also explain why mitochondrial transmembrane potential was disturbed in CSE-treated ARPE-19 cells. It was reported that depolarization via mitochondrial uncoupling reduces mitochondrial ROS production and hyperpolarization promotes ROS generation and oxidative damage [58–61]. Unexpectedly, we observed enlarged, elongated mitochondria accompanied by no change in mitochondrial mass in ARPE-19 cells treated with 5% CSE compared to non-treated controls, which is an unusual phenotype when membrane potential is lost and ATP production ceases. Usually, such pathological changes of mitochondrial integrity would activate mitochondrial fission, which promotes mitophagy [62]. Thus far, it is unclear whether there is a causal relationship between mitochondrial transmembrane potential, ROS and mitochondrial morphology observed upon CSE-treatment in our study model. However, we can infer from our results that CSE treatment causes a marked disruption of mitochondrial integrity and, as a consequence, mitochondrial respiration. In accordance with these findings, Seahorse analyses revealed impaired OXPHOS in cells treated with 5% CSE without a compensatory switch to glycolysis, which would be expected in such an energy-deprived state [40–42]. We were able to restore glycolytic capacity by either incubating the cells under hypoxic conditions or treatment with Roxadustat, providing a direct link between CSE-dependent metabolic dysregulation and HIF-1α degradation under normoxia. Future research should also address whether CSE-induced downregulation of glycolytic flux is caused by disruption of the transcriptional activity of HIF-1 or by a recently reported mechanism by which HIF-1α is involved in the cytoplasmic formation of a metabolic complex involving several glycolytic enzymes [63].

In summary, we found dysregulated HIF signaling in CSE-treated cells under normoxic conditions, which also had functional implications for ARPE-19 cells as not only OXPHOS but also glycolysis was impaired. While impairment of OXPHOS was not HIF-dependent, the lack of a compensatory switch to glycolysis was caused by HIF destabilization under normoxia (Fig. 5). Most interestingly, there is still not much known about the role and regulation of HIFs under normoxic conditions beyond cancer cells and our findings provide important data on the regulation of glycolysis under the control of HIFs under normoxic conditions. In healthy RPE cells, mitochondrial respiration is the main source of ATP synthesis. Therefore, upregulating the glycolytic rate without restoring OXPHOS, as conducted in this study, would result in two major problems when translated into the in vivo situation. First, glycolysis alone is not sufficient to cover the metabolic demand of RPE cells, and second, RPE cells would metabolize far more glucose to fuel their own glycolysis, which would lead to a glucose shortage in glucose-dependent photoreceptor cells. Investigation of these systemic associations will be the subject of future studies.

MATERIAL AND METHODS
Cell culture
Human RPE cells (ARPE-19, CRL-2302, American Type Culture Collection, Manassas, VA; distributed by LGC Standards GmbH, Wesel, Germany) were routinely cultivated in Dulbecco's modified Eagle's medium (DMEM)/F-12 (11330057, Thermo Fisher Scientific), supplemented with 10 % FBS and penicillin–streptomycin in a humidified incubator at 37 °C with 5% CO_2. All experiments were conducted with DMEM/F12 supplemented with 1% FBS.
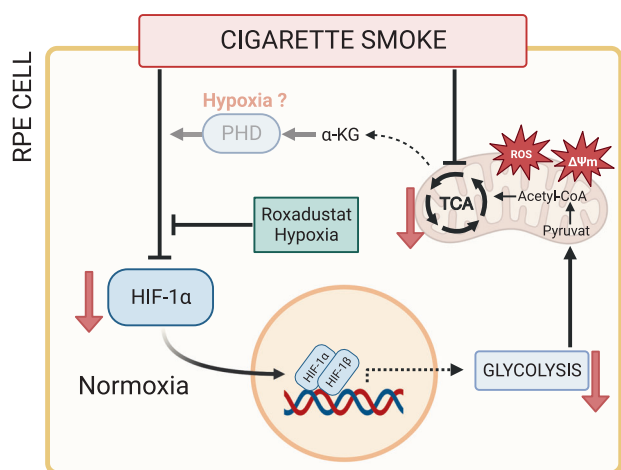
Fig. 5 Conclusion. In the present study, treatment of ARPE-19 cells with CSE was shown to downregulate mitochondrial respiration, presumably by TCA cycle inhibition indicated by increased α-ketoglutarate (α-KG) levels in CSE-treated cells under normoxic conditions (21% O_2). CSE treatment also affected mitochondrial morphology and increased mitochondrial ROS as well as mitochondrial membrane potential (hyperpolarization). Glycolysis could not fully compensate for impaired mitochondrial respiration, because CSE inhibited glycolysis indirectly by downregulating HIF-1α protein levels under normoxia, resulting in a bioenergetic crisis, because two major metabolic pathways to generate ATP are inhibited by CSE. At least glycolysis was restored by incubation of cells under hypoxia (1% O_2) or with Roxadustat, which both induce HIF stabilization. These findings point out that HIF-1 is also responsible for the regulation of glycolysis under normoxic conditions in ARPE-19 cells. HIF-1α was also downregulated by CSE under hypoxic conditions, but downstream effects of CSE-induced HIF-1α downregulation were only observed under normoxic conditions. Moreover, while downregulation of HIF-1α under hypoxia was accompanied by increased HIF-1α hydroxylation by PHDs (possibly induced by higher α-KG levels), hydroxy-HIF-1α was even downregulated by CSE under normoxic conditions, suggesting that CSE acts differentially on HIF-1α protein depending on oxygen availability. Red arrows depict CSE-induced effects. The figure was created with BioRender.com.

Cells were authenticated by STR profiling and routinely tested for mycoplasma contamination. All experiments were conducted within five passages.

HIF stabilization
For HIF stabilization, cells were either treated under hypoxia or with Roxadustat, a clinically approved PHD inhibitor [64], under normoxia (21% O_2). Hypoxia was achieved by incubating the cells in a hypoxic chamber at 1% O_2 for the indicated time. For Roxadustat treatment, a stock solution of 10 mM in DMSO was diluted to a final concentration of 30 µM in a cell culture medium.

Preparation of cigarette smoke extract
CSE was prepared by bubbling the smoke from four filter cigarettes (Marlboro; Philip Morris Products, Neuchatel, Switzerland; nicotine 0.9 mg, tar 12 mg) through 30 ml cell culture medium without additives (DMEM/F-12 with GlutaMax, Gibco) with a vacuum pump. Each cigarette was smoked in 10 puffs with 30 s breaks. 75% of each cigarette was smoked. This corresponds to a smoke length of 4.7 cm and a tobacco quantity of 530 mg with a theoretical nicotine content of 53.2 mg. The exposure quantity calculation was based on the results of Bernhard et al. [65].

Western blot
Cells were seeded in six-well plates at a density of 200,000 cells/well and grown to confluence. For protein isolation, cells were washed with cold PBS, collected in lysis buffer using a cell scraper, incubated on ice for 20 min, and centrifuged for 5 min at 500 rpm. The supernatant was stored at −80 °C until use. 30 µg of total protein were incubated in Laemmli

sample buffer for 5 min at 95 °C and subjected to SDS–PAGE. Separated proteins were transferred to a PVDF membrane with a Trans-Blot Turbo Transfer System (Bio-Rad Laboratories, Feldkirchen, Germany). Membranes were blocked with 5% skim milk in TBS-T for 1 h at room temperature. Primary antibodies against HIF-1α (610958, BD Biosciences, Franklin Lakes, NJ), hydroxy-HIF-1α (3434, Cell Signaling Technology, Danvers, MA), HIF-2α (NB100-122, Novus Biologicals, Littleton, CO), TOM20 (11802-1-AP, Proteintech Group, Rosemont, IL), HSP60 (15282-1-AP, Proteintech Group), and Tubulin (sc-8035, Santa Cruz Biotechnology, Dallas, TX) were diluted in blocking buffer and incubated overnight at 4 °C. To detect proteins, goat anti-mouse (A2304, Sigma Aldrich, St. Louis, MO, USA) and goat anti-rabbit (A0545, Sigma Aldrich) secondary antibodies were diluted in a blocking buffer and incubated for 1 h at room temperature. Signals were developed with SuperSignal West Femto Maximum Sensitivity Substrate (34096, Thermo Fisher Scientific), detected with a Fusion FX System (Vilber, Eberhardzell, Germany), and quantified with ImageJ. Full-length uncropped original western blots are provided in Supplemental Material (Supplementary File 1).

Quantitative real-time PCR
Total RNA was isolated using the NucleoSpin RNA kit (740955.250, Macherey-Nagel, Düren Germany) according to the manufacturer's instructions. Complementary DNA (cDNA) was synthesized from 500 ng total RNA using M-MLV reverse transcriptase (M1705, Promega, Walldorf, Germany) and oligo dT primer. Quantitative Real-Time PCR (qRT-PCR) was performed with a Biozym Blue S'Green master mix (331416XL, Biozym Scientific, Hessisch Oldendorf, Germany) on a BioRad CFX Opus 96 System. Relative expression levels were calculated with the ΔΔct method using *hypoxanthine-guanine phosphoribosyltransferase* (*HPRT*) as a reference gene. The following primer pairs were used: *HIF1A* 5′-GGATGCTGGTGATTT GGATA-3′ (forward) and 5′-TCATGGTCACATGGATGAGTA-3′ (reverse); *HIF2A* 5′-CGGAGGTGTTCTATGAGCTGG-3′ (forward) and 5′-AGCTTGTGTGTTCGCA GGAA-3′ (reverse); *CA9* 5′-CACGTGGTTCACCTCAGCAC-3′ (forward) and 5′-CAGCGATTTCTTCCAAGCG-3′ (reverse); *HPRT* 5′-CCTGGCGTCGTGATTAGT GA-3′ (forward) and 5′-CGAGCAAGACGTTCAGTCCT-3′ (reverse).

Flow cytometry analysis of reactive oxygen species and mitochondrial membrane potential
Cells were plated in six-well plates at a density of 200,000 cells/well. Confluent cells were treated with CSE for indicated time periods. The supernatants were collected in flow cytometry tubes before detaching the cells with accutase (PAN Biotech, Germany). Accutase reaction was stopped by the addition of cell culture media. Detached cells were transferred to flow cytometry tubes and centrifuged at 1500 rpm at room temperature. The supernatant was discarded and cell pellets were separately stained with the following staining solutions for different purposes as previously described [66–68]. Mitochondrial ROS production was assessed by staining the cells with 5 µM of MitoSOX (Molecular Probes/Invitrogen, Carlsbad, CA, USA) for 30 min at 37 °C. To analyze mitochondrial membrane potential, cell pellets were stained using 25 nM of the potential-specific dye tetramethyl rhodamine ethyl ester (TMRE; Molecular Probes/Invitrogen, Carlsbad, CA, USA) for 30 min at 37 °C as previously described [69]. TMRE staining allows for measuring dissipation of the mitochondrial membrane potential (ΔΨm) as depolarized or inactive mitochondria have decreased membrane potential and fail to bind TMRE. Readouts were accessed by flow cytometry (CytoFLEX S, Beckman Coulter).

MitoTracker deep red staining
To visualize mitochondrial membrane potential, cells were treated with 5% CSE for 8 h and afterward incubated with fresh cell culture medium containing MitoTracker Deep Red FM (1:5000; Molecular Probes/Invitrogen, Carlsbad, CA, USA), a polarization-dependent fluorescence staining of mitochondria [38, 39], for 15 min in the dark. Cells were washed and fixed with 3% paraformaldehyde containing 0.2% Triton X-100 in PBS. For counterstaining, cells were incubated with Phalloidin-TRITC (1:200) and embedded with Mowiol containing DAPI (1:1000). Fluorescence imaging was conducted with a Zeiss Axio Observer Z1 fluorescence microscope with ApoTome and ZEN imaging software (Carl Zeiss, Goettingen, Germany).

Extracellular flux assay—mitochondrial stress test
Cells were plated at a density of 7500 cells/well in XF96 micro-plates (Agilent Technologies, Santa Clara, CA, USA) in DMEM/F12 supplemented

with 10% FBS 48 h prior to the assay and cultivated in a humified incubator at 37 °C with 5% CO$_2$. All treatments were conducted in DMEM/F12 with 1% FBS for the indicated time. 1 h prior to the assay time point, the medium was exchanged to the Seahorse XF Base Medium (Agilent Technologies) with 1 mM sodium pyruvate, 2 mM L-glutamine and 10 mM D-(+)-glucose (all Sigma-Aldrich), pH 7.4 and incubated at 37 °C without CO$_2$. During assays, oxygen consumption rate (OCR) and extracellular acidification rate (ECAR) were measured in parallel using a Seahorse XFe96 Analyzer (Agilent Technologies). Seahorse XF Cell Mito Stress Test kit (Agilent Technologies) containing injections of oligomycin (1 μM), carbonyl cyanide-4-(trifluoromethoxy) phenylhydrazone (FCCP, 0.25 μM), followed by combined injection of rotenone and antimycin A (0.5 μM) was performed according to manufacturer's protocol. For individual well normalization of cell number, DNA content fluorescence was measured after cells were stained with 10 mg/mL Hoechst 33342 (Sigma-Aldrich) solution after each assay. Data were analyzed using Wave 2.6 software (Agilent Technologies). Mean values of $n = 13$–52 wells per experimental group from a total $N = 3$–7 independent experiments were used for the analysis as previously described [70, 71]. All metabolic parameters were normalized to Hoechst intensity (relative fluorescence units, RFU) in each well.

Extracellular flux assay—glycolysis rate assay
Cells were plated at a density of 7500 cells/well in XF96 micro-plates (Agilent Technologies) in DMEM/F12 supplemented with 10% FBS 48 h prior to the assay and cultivated in a humified incubator at 37 °C with 5% CO$_2$. All treatments were conducted in DMEM/F12 with 1% FBS for the indicated time. For Glycolytic Rate Assay, the medium was exchanged to XF DMEM medium (Agilent Technologies) with 2 mM glutamine, 10 mM glucose, 1 mM pyruvate, and 5 mM HEPES and incubated at 37 °C without CO$_2$ 1 h prior to the assay. During the assay, the extracellular acidification rate (ECAR) was measured using a Seahorse XFe96 Analyzer. Glycolytic Rate Assay Kit containing 0.5 μM Rotenone, 0.5 μM Antimycin A, and 50 mM 2-Desoxyglucose was performed according to the manufacturer's protocol. Proton efflux rate (PER) was calculated by Wave 2.6 (Agilent Technologies) software after the assay. Normalization of the cell number and data evaluation using Wave 2.6 software was performed as described above for the mitochondrial stress test.

LDH assay
To assess cell viability, LDH release was measured using a CyQUANT™ LDH Cytotoxicity Assay (C20301, Thermo Fisher Scientific). Briefly, cells were seeded at a density of 10,000 cells/well in a 96-well plate. Confluent cells were treated with different CSE concentrations for 24 h. Subsequently, 50 μL of cell culture medium was transferred to a 96-well plate and subjected to LDH measurement according to the manufacturer's instructions. Absorbance was measured at 490 nm with a plate reader.

Measurement of α-ketoglutarate
Intracellular α-ketoglutarate was measured using a colorimetric α-ketoglutarate assay (MET-5131, Cell Biolabs Inc., San Diego, CA) according to the manufacturer's instructions. In brief, ARPE-19 cells were treated with 5% CSE for 24 h and subsequently homogenized in assay buffer before centrifugation at 12,000×g for 10 min to collect the supernatant. To avoid oxidation of the samples, superoxide dismutase (S9697, Sigma Aldrich) at a final concentration of 40 U/mL was added to the samples. Samples were incubated for 2 h with the reaction reagent and absorbance was measured at 540 nm.

Transmission electron microscopy
For transmission electron microscopy (TEM), ARPE-19 cells were seeded in T25 flasks and grown to confluence. Confluent cells were treated with 0%, 1%, 3%, and 5% CSE for 16 h. Subsequently, after treatment, cells were fixed with 2% glutaraldehyde (#G5882, Merck, Darmstadt, Germany) in 0.1 M cacodylate buffer for 1.5 h. After cells were washed with phosphate buffer (PB), samples were stained with 1% osmium tetroxide in H$_2$O for 1 h. Thereafter, cells were detached from the flask's bottom with cell scrapers and centrifuged at 1041×g for 10 min. Afterward, cell pellets were embedded in Agar–Agar (4% in PB). Next, specimens were dehydrated through an ascending ethanol series, starting with 50% ethanol, followed by incubation in 70% ethanol, 1% uranyl acetate (#21447, Polyscience Europe, Heidelberg, Germany), and 1% phosphotungstic acid (#455970, Merck, Darmstadt, Germany) solution overnight at 4 °C. Dehydration

continued with an ascending ethanol series (80–100%). Afterward the samples were first incubated in propylene oxide (#807027, Merck, Germany), followed by an ascending series of propylene oxide and EPON mixtures. EPON consists of glycidether (#21045.02, Serva, Heidelberg, Germany), methylnadic anhydride (#29452.02, Serva, Heidelberg, Germany), 2-dodecenylsuccinic acid anhydride (#20755.01, Serva, Heidelberg, Germany) and 2,4,6-Tris(dimethylaminomethyl)phenol (#36975.01, Serva, Heidelberg, Germany) in a 5.4:3.8:1.84:1 mixture. The embedding procedure started with propylene oxide/EPON in a 3:1 ratio, followed by a 1:1 ratio, and ended with a 1:3 ratio. Finally, specimens were penetrated by pure EPON overnight at 20 °C. On the next day, EPON was renewed. The EPON-embedded specimens were allowed to polymerize at 60 °C for 2 days. 50 nm sections were cut with an Ultracut E Reichert-Jung (Leica Microsystems GmbH, Wetzlar, Germany) with a DiATOME histo diamond knife (45°, 6 mm, MX559; Diatome AG, Nidau, Switzerland), collected on Formvar-coated grids and contrasted with UranylLess (#22409, Electron Microscopy Sciences, Hatfield, USA) for 5 min. Samples were analyzed with a Zeiss LEO 910 transmission electron microscope equipped with a digital CCD camera. ImageJ 1.51 s (National Institutes of Health, Bethesda, MD, USA) was used for the evaluation of single mitochondrial morphological parameters (area, perimeter, circularity, Ferret's diameter, aspect ratio, and roundness).

Statistical analysis
Statistical analyses were performed using GraphPad Prism (vers. 9.3.1, San Diego, CA, USA). All data were tested for normal distribution using three normality tests (Anderson–Darling, D'Agostino–Pearson omnibus, and Shapiro–Wilk). Data were log-transformed when datasets were not normally distributed. In case, normal distribution was not achieved by log-transformation, non-parametrical tests were applied. Unpaired t-tests were applied to compare two groups, three or more groups were compared with a one-way ANOVA followed by Tukey's or Dunnett's multiple comparisons test, and two-factor analyses were conducted with a mixed-effects model followed by Šídák's or Tukey's multiple comparisons test. Sample sizes were chosen according to the recommendations of Naegle et al. [72] and are indicated in the respective figure legends. All data are expressed as mean ± SD. Statistical significance was defined as *$p < 0.05$; **$p < 0.01$, ***$p < 0.001$, and ****$p < 0.0001$.

DATA AVAILABILITY
Data generated and analyzed during the current study will be made available upon request.

REFERENCES
1. Strauss O. The retinal pigment epithelium in visual function. Physiol Rev. 2005;85:845–81. https://doi.org/10.1152/physrev.00021.2004.
2. Pan WW, Wubben TJ, Besirli CG. Photoreceptor metabolic reprogramming: current understanding and therapeutic implications. Commun Biol 2021;4:245. https://doi.org/10.1038/s42003-021-01765-3.
3. Hurley JB. Retina metabolism and metabolism in the pigmented epithelium: a busy intersection. Annu Rev Vis Sci 2021;7:665–92. https://doi.org/10.1146/annurev-vision-100419-115156.
4. Fernandes AR, Zielińska A, Sanchez-Lopez E, dos Santos T, Garcia ML, Silva AM, et al. Exudative versus nonexudative age-related macular degeneration: physiopathology and treatment options. Int J Mol Sci 2022;23:2592. https://doi.org/10.3390/ijms23052592.
5. Wong WL, Su X, Li X, Cheung CMG, Klein R, Cheng C-Y, et al. Global prevalence of age-related macular degeneration and disease burden projection for 2020 and 2040: a systematic review and meta-analysis. Lancet Glob Health. 2014;2:e106–e116. https://doi.org/10.1016/S2214-109X(13)70145-1.
6. Stahl A. The diagnosis and treatment of age-related macular degeneration. Dtsch Arztebl Int 2020;117:513–20. https://doi.org/10.3238/arztebl.2020.0513.
7. Cabral de Guimaraes TA, Daich Varela M, Georgiou M, Michaelides M. Treatments for dry age-related macular degeneration: therapeutic avenues, clinical trials and future directions. Br J Ophthalmol 2021;106:297–304. https://doi.org/10.1136/bjophthalmol-2020-318452.
8. Dallinger S, Findl O, Strenn K, Eichler HG, Wolzt M, Schmetterer L. Age dependence of choroidal blood flow. J Am Geriatr Soc 1998;46:484–7. https://doi.org/10.1111/j.1532-5415.1998.tb02471.x.
9. Velilla S, García-Medina JJ, García-Layana A, Dolz-Marco R, Pons-Vázquez S, Pinazo-Durán MD, et al. Smoking and age-related macular degeneration: review and update. J Ophthalmol 2013;2013:895147. https://doi.org/10.1155/2013/895147.

10. Tong Y, Zhang Z, Wang S. Role of mitochondria in retinal pigment epithelial aging and degeneration. Front Aging 2022;3. https://doi.org/10.3389/fragi.2022.926627.

11. Greijer AE, van der Groep P, Kemming D, Shvarts A, Semenza GL, Meijer GA, et al. Up-regulation of gene expression by hypoxia is mediated predominantly by hypoxia-inducible factor 1 (HIF-1). J Pathol 2005;206:291–304. https://doi.org/10.1002/path.1778.

12. Semenza GL, Agani F, Booth G, Forsythe J, Iyer N, Jiang BH, et al. Structural and functional analysis of hypoxia-inducible factor 1. Kidney Int. 1997;51:553–5. https://doi.org/10.1038/ki.1997.77.

13. Fandrey J, Gorr TA, Gassmann M. Regulating cellular oxygen sensing by hydroxylation. Cardiovasc Res 2006;71:642–51. https://doi.org/10.1016/j.cardiores.2006.05.005.

14. Leu T, Schützhold V, Fandrey J, Ferenz KB. When the brain yearns for oxygen. Neurosignals. 2019;27:50–61. https://doi.org/10.33594/000000199.

15. Arjamaa O, Nikinmaa M, Salminen A, Kaarniranta K. Regulatory role of HIF-1alpha in the pathogenesis of age-related macular degeneration (AMD). Ageing Res Rev 2009;8:349–58. https://doi.org/10.1016/j.arr.2009.06.002.

16. Lange CA, Bainbridge JW. Oxygen sensing in retinal health and disease. Ophthalmologica. 2012;227:115–31. https://doi.org/10.1159/000331418.

17. Barben M, Schori C, Samardzija M, Grimm C. Targeting *Hif1a* rescues cone degeneration and prevents subretinal neovascularization in a model of chronic hypoxia. Mol Neurodegener 2018;13. https://doi.org/10.1186/s13024-018-0243-y.

18. Peters F, Ebner LJA, Atac D, Maggi J, Berger W, den Hollander AI, et al. Regulation of ABCA1 by AMD-associated genetic variants and hypoxia in iPSC-RPE. Int J Mol Sci 2022;23. https://doi.org/10.3390/ijms23063194.

19. Ferrington DA, Ebeling MC, Kapphahn RJ, Terluk MR, Fisher CR, Polanco JR, et al. Altered bioenergetics and enhanced resistance to oxidative stress in human retinal pigment epithelial cells from donors with age-related macular degeneration. Redox Biol. 2017;13:255–65. https://doi.org/10.1016/j.redox.2017.05.015.

20. Zhang M, Jiang N, Chu Y, Postnikova O, Varghese R, Horvath A, et al. Dysregulated metabolic pathways in age-related macular degeneration. Sci Rep 2020;10:2464. https://doi.org/10.1038/s41598-020-59244-4.

21. Kaarniranta K, Uusitalo H, Blasiak J, Felszeghy S, Kannan R, Kauppinen A, et al. Mechanisms of mitochondrial dysfunction and their impact on age-related macular degeneration. Prog Retin Eye Res 2020;79:100858. https://doi.org/10.1016/j.preteyeres.2020.100858.

22. Nolan ND, Caruso SM, Cui X, Tsang SH. Renormalization of metabolic coupling treats age-related degenerative disorders: an oxidative RPE niche fuels the more glycolytic photoreceptors. Eye. 2022;36:278–83. https://doi.org/10.1038/s41433-021-01726-4.

23. Brown EE, DeWeerd AJ, Ildefonso CJ, Lewin AS, Ash JD. Mitochondrial oxidative stress in the retinal pigment epithelium (RPE) led to metabolic dysfunction in both the RPE and retinal photoreceptors. Redox Biol. 2019;24:101201. https://doi.org/10.1016/j.redox.2019.101201.

24. Kurihara T, Westenskow PD, Gantner ML, Usui Y, Schultz A, Bravo S, et al. Hypoxia-induced metabolic stress in retinal pigment epithelial cells is sufficient to induce photoreceptor degeneration. eLife. 2016;5:e14319. https://doi.org/10.7554/eLife.14319.

25. Léveillard T, Philp NJ, Sennlaub F. Is retinal metabolic dysfunction at the center of the pathogenesis of age-related macular degeneration? Int J Mol Sci 2019;20:762.

26. Ebeling MC, Polanco JR, Qu J, Tu C, Montezuma SR, Ferrington DA. Improving retinal mitochondrial function as a treatment for age-related macular degeneration. Redox Biol. 2020;34:101552. https://doi.org/10.1016/j.redox.2020.101552.

27. Fisher CR, Ferrington DA. Perspective on AMD pathobiology: a bioenergetic crisis in the RPE. Investig Ophthalmol Vis Sci 2018;59:Amd41–amd47. https://doi.org/10.1167/iovs.18-24289.

28. Thornton J, Edwards R, Mitchell P, Harrison RA, Buchan I, Kelly SP. Smoking and age-related macular degeneration: a review of association. Eye (London). 2005;19:935–44. https://doi.org/10.1038/sj.eye.6701978.

29. Huang C, Wang JJ, Ma JH, Jin C, Yu Q, Zhang SX. Activation of the UPR protects against cigarette smoke-induced RPE apoptosis through up-regulation of Nrf2. J Biol Chem 2015;290:5367–80. https://doi.org/10.1074/jbc.M114.603738.

30. Bertram KM, Baglole CJ, Phipps RP, Libby RT. Molecular regulation of cigarette smoke induced-oxidative stress in human retinal pigment epithelial cells: implications for age-related macular degeneration. Am J Physiol Cell Physiol 2009;297:C1200–1210. https://doi.org/10.1152/ajpcell.00126.2009.

31. Cano M, Datta S, Wang L, Liu T, Flores-Bellver M, Sachdeva M, et al. Nrf2 deficiency decreases NADPH from impaired IDH shuttle and pentose phosphate pathway in retinal pigmented epithelial cells to magnify oxidative stress-induced mitochondrial dysfunction. Aging Cell. 2021;20:e13444. https://doi.org/10.1111/acel.13444.

32. Hoffmann RF, Zarrintan S, Brandenburg SM, Kol A, de Bruin HG, Jafari S, et al. Prolonged cigarette smoke exposure alters mitochondrial structure and function in airway epithelial cells. Respir Res 2013;14:97. https://doi.org/10.1186/1465-9921-14-97.

33. Aghapour M, Tulen CBM, Abdi Sarabi M, Weinert S, Müsken M, Relja B, et al. Cigarette smoke extract disturbs mitochondria-regulated airway epithelial cell responses to pneumococci. Cells. 2022;11:1771. https://doi.org/10.3390/cells11111771.

34. Ito S, Araya J, Kurita Y, Kobayashi K, Takasaka N, Yoshida M, et al. PARK2-mediated mitophagy is involved in regulation of HBEC senescence in COPD pathogenesis. Autophagy. 2015;11:547–59. https://doi.org/10.1080/15548627.2015.1017190.

35. Maremanda KP, Sundar IK, Rahman I. Role of inner mitochondrial protein OPA1 in mitochondrial dysfunction by tobacco smoking and in the pathogenesis of COPD. Redox Biol. 2021;45:102055. https://doi.org/10.1016/j.redox.2021.102055.

36. Li L, Liu Y, Liu X, Zheng N, Gu Y, Song Y, et al. Regulatory roles of external cholesterol in human airway epithelial mitochondrial function through STARD3 signalling. Clin Transl Med 2022;12:e902. https://doi.org/10.1002/ctm2.902.

37. Görtz GE, Horstmann M, Aniol B, Reyes BD, Fandrey J, Eckstein A, et al. Hypoxia-dependent HIF-1 activation impacts on tissue remodeling in Graves' ophthalmopathy—implications for smoking. J Clin Endocrinol Metab 2016;101:4834–42. https://doi.org/10.1210/jc.2016-1279.

38. Monteiro LdB, Davanzo GG, de Aguiar CF, Moraes-Vieira PMM. Using flow cytometry for mitochondrial assays. MethodsX. 2020;7:100938. https://doi.org/10.1016/j.mex.2020.100938.

39. Xiao B, Deng X, Zhou W, Tan E-K. Flow cytometry-based assessment of mitophagy using mitotracker. Front Cell Neurosci 2016;10. https://doi.org/10.3389/fncel.2016.00076/

40. Fu Y, Wang D, Wang H, Cai M, Li C, Zhang X, et al. TSPO deficiency induces mitochondrial dysfunction, leading to hypoxia, angiogenesis, and a growth-promoting metabolic shift toward glycolysis in glioblastoma. Neuro Oncol 2020;22:240–52. https://doi.org/10.1093/neuonc/noz183.

41. Sánchez-González C, Nuevo-Tapioles C, Herrero Martín JC, Pereira MP, Serrano Sanz S, Ramírez de Molina A, et al. Dysfunctional oxidative phosphorylation shunts branched-chain amino acid catabolism onto lipogenesis in skeletal muscle. EMBO J. 2020;39:e103812. https://doi.org/10.15252/embj.2019103812.

42. Ait-Aissa K, Blaszak SC, Beutner G, Tsaih S-W, Morgan G, Santos JH, et al. Mitochondrial oxidative phosphorylation defect in the heart of subjects with coronary artery disease. Sci Rep 2019;9:7623. https://doi.org/10.1038/s41598-019-43761-y.

43. Kierans SJ, Taylor CT. Regulation of glycolysis by the hypoxia-inducible factor (HIF): implications for cellular physiology. J Physiol 2021;599:23–37. https://doi.org/10.1113/jp280572.

44. Kaelin WG, Ratcliffe PJ. Oxygen sensing by metazoans: the central role of the HIF hydroxylase pathway. Mol Cell. 2008;30:393–402. https://doi.org/10.1016/j.molcel.2008.04.009.

45. Lum JJ, Bui T, Gruber M, Gordan JD, DeBerardinis RJ, Covello KL, et al. The transcription factor HIF-1alpha plays a critical role in the growth factor-dependent regulation of both aerobic and anaerobic glycolysis. Genes Dev. 2007;21:1037–49. https://doi.org/10.1101/gad.1529107.

46. Iyer NV, Kotch LE, Agani F, Leung SW, Laughner E, Wenger RH, et al. Cellular and developmental control of O₂ homeostasis by hypoxia-inducible factor 1 alpha. Genes Dev. 1998;12:149–62. https://doi.org/10.1101/gad.12.2.149.

47. Del Rey MJ, Valín Á, Usategui A, García-Herrero CM, Sánchez-Aragó M, Cuezva JM, et al. Hif-1α knockdown reduces glycolytic metabolism and induces cell death of human synovial fibroblasts under normoxic conditions. Sci Rep 2017;7:3644. https://doi.org/10.1038/s41598-017-03921-4.

48. K. Trofimova L, L. Araujo W, A. Strokina A, R. Fernie A, Bettendorff L, I. Bunik V. Consequences of the α-ketoglutarate dehydrogenase inhibition for neuronal metabolism and survival: implications for neurodegenerative diseases. Curr Med Chem 2012;19:5895–906. https://doi.org/10.2174/092986712804143367.

49. Shi Q, Xu H, Kleinman WA, Gibson GE. Novel functions of the α-ketoglutarate dehydrogenase complex may mediate diverse oxidant-induced changes in mitochondrial enzymes associated with Alzheimer's disease. Biochim Biophys Acta Mol Basis Dis 2008;1782:229–38. https://doi.org/10.1016/j.bbadis.2007.12.008.

50. Strowitzki MJ, Cummins EP, Taylor CT. Protein hydroxylation by hypoxia-inducible factor (HIF) hydroxylases: unique or ubiquitous? Cells. 2019;8:384.

51. Tennant DA, Frezza C, MacKenzie ED, Nguyen QD, Zheng L, Selak MA, et al. Reactivating HIF prolyl hydroxylases under hypoxia results in metabolic catastrophe and cell death. Oncogene. 2009;28:4009–21. https://doi.org/10.1038/onc.2009.250.

52. Appelhoff RJ, Tian Y-M, Raval RR, Turley H, Harris AL, Pugh CW, et al. Differential function of the prolyl hydroxylases PHD1, PHD2, and PHD3 in the regulation of hypoxia-inducible factor. J Biol Chem 2004;279:38458–65. https://doi.org/10.1074/jbc.M406026200.

53. Wong SJ, Ringel AE, Yuan W, Paulo JA, Yoon H, Currie MA, et al. Development of a colorimetric α-ketoglutarate detection assay for prolyl hydroxylase domain (PHD) proteins. J Biol Chem 2021;296:100397. https://doi.org/10.1016/j.jbc.2021.100397.

54. Laukka T, Mariani CJ, Ihantola T, Cao JZ, Hokkanen J, Kaelin WG, et al. Fumarate and succinate regulate expression of hypoxia-inducible genes via TET enzymes. J Biol Chem 2016;291:4256–65. https://doi.org/10.1074/jbc.M115.688762.

55. Selak MA, Armour SM, MacKenzie ED, Boulahbel H, Watson DG, Mansfield KD, et al. Succinate links TCA cycle dysfunction to oncogenesis by inhibiting HIF-α prolyl hydroxylase. Cancer Cell. 2005;7:77–85. https://doi.org/10.1016/j.ccr.2004.11.022.

56. Chouchani ET, Pell VR, Gaude E, Aksentijević D, Sundier SY, Robb EL, et al. Ischaemic accumulation of succinate controls reperfusion injury through mitochondrial ROS. Nature. 2014;515:431–5. https://doi.org/10.1038/nature13909.

57. Robb EL, Hall AR, Prime TA, Eaton S, Szibor M, Viscomi C, et al. Control of mitochondrial superoxide production by reverse electron transport at complex I. J Biol Chem 2018;293:9869–79. https://doi.org/10.1074/jbc.RA118.003647.

58. Esteras N, Rohrer JD, Hardy J, Wray S, Abramov AY. Mitochondrial hyperpolarization in iPSC-derived neurons from patients of FTDP-17 with 10+16 MAPT mutation leads to oxidative stress and neurodegeneration. Redox Biol. 2017;12:410–22. https://doi.org/10.1016/j.redox.2017.03.008.

59. Korshunov SS, Skulachev VP, Starkov AA. High protonic potential actuates a mechanism of production of reactive oxygen species in mitochondria. FEBS Lett. 1997;416:15–18. https://doi.org/10.1016/S0014-5793(97)01159-9.

60. Poppe M, Reimertz C, Düßmann H, Krohn AJ, Luetjens CM, Böckelmann D, et al. Dissipation of potassium and proton gradients inhibits mitochondrial hyperpolarization and cytochrome c release during neural apoptosis. J Neurosci 2001;21:4551–63. https://doi.org/10.1523/jneurosci.21-13-04551.2001.

61. Andrews ZB, Horvath B, Barnstable CJ, Elseworth J, Yang L, Beal MF, et al. Uncoupling protein-2 Is critical for nigral dopamine cell survival in a mouse model of Parkinson's disease. J Neurosci 2005;25:184–91. https://doi.org/10.1523/jneurosci.4269-04.2005.

62. Bordi M, Nazio F, Campello S. The close interconnection between mitochondrial dynamics and mitophagy in cancer. Front Oncol 2017;7. https://doi.org/10.3389/fonc.2017.00081.

63. Kierans SJ, Fagundes RR, Malkov MI, Sparkes R, Dillon ET, Smolenski A, et al. Hypoxia induces a glycolytic complex in intestinal epithelial cells independent of HIF-1-driven glycolytic gene expression. Proc Natl Acad Sci USA 2023;120:e2208117120. https://doi.org/10.1073/pnas.2208117120.

64. Dhillon S. Roxadustat: first global approval. Drugs. 2019;79:563–72. https://doi.org/10.1007/s40265-019-01077-1.

65. Bernhard D, Huck CW, Jakschitz T, Pfister G, Henderson B, Bonn GK, et al. Development and evaluation of an in vitro model for the analysis of cigarette smoke effects on cultured cells and tissues. J Pharmacol Toxicol Methods. 2004;50:45–51. https://doi.org/10.1016/j.vascn.2004.01.003.

66. Hansel C, Hlouschek J, Xiang K, Melnikova M, Thomale J, Helleday T et al. Adaptation to chronic-cycling hypoxia renders cancer cells resistant to MTH1-inhibitor treatment which can be counteracted by glutathione depletion. Cells 2021;10. https://doi.org/10.3390/cells10113040.

67. Xiang K, Kalthoff C, Munch C, Jendrossek V, Matschke J. Accumulation of oncometabolite D-2-hydroxyglutarate by SLC25A1 inhibition: a metabolic strategy for induction of HR-ness and radiosensitivity. Cell Death Dis. 2022;13:641. https://doi.org/10.1038/s41419-022-05098-9.

68. Hlouschek J, Hansel C, Jendrossek V, Matschke J. The mitochondrial citrate Carrier (SLC25A1) sustains redox homeostasis and mitochondrial metabolism supporting radioresistance of cancer cells with tolerance to cycling severe hypoxia. Front Oncol 2018;8:170. https://doi.org/10.3389/fonc.2018.00170.

69. Matschke J, Riffkin H, Klein D, Handrick R, Ludemann L, Metzen E, et al. Targeted inhibition of glutamine-dependent glutathione metabolism overcomes death resistance induced by chronic cycling hypoxia. Antioxid Redox Signal 2016;25:89–107. https://doi.org/10.1089/ars.2015.6589.

70. Divakaruni AS, Paradyse A, Ferrick DA, Murphy AN, Jastroch M. Chapter Sixteen - Analysis and Interpretation of Microplate-Based Oxygen Consumption and pH Data. In: Murphy AN, Chan DC, editors. Methods in enzymology. vol. 547, p. 309–54 (Academic Press, Waltham, San Diego, London, Oxford; 2014). https://www.sciencedirect.com/bookseries/methods-in-enzymology/vol/547/suppl/C.

71. Krysztofiak A, Szymonowicz K, Hlouschek J, Xiang K, Waterkamp C, Larafa S, et al. Metabolism of cancer cells commonly responds to irradiation by a transient early mitochondrial shutdown. iScience. 2021;24:103366. https://doi.org/10.1016/j.isci.2021.103366.

72. Naegle K, Gough NR, Yaffe MB. Criteria for biological reproducibility: what does "n" mean? Sci Signal 2015;8:fs7. https://doi.org/10.1126/scisignal.aab1125.

AUTHOR CONTRIBUTIONS

Conceived the study and experimental design: YH, G-EG, JM. Performed experiments: YH, KW, GW, SL, VM, CT, G-EG, and JM. Analyzed and interpreted data: YH, KW, GW, SL, VM, G-EG, and JM. Wrote the manuscript: YH with significant input from all co-authors. All authors read and approved the manuscript.

COMPETING INTERESTS

The authors declare no competing interests.

ADDITIONAL INFORMATION

Supplementary information The online version contains supplementary material available at https://doi.org/10.1038/s41420-023-01695-5.

Correspondence and requests for materials should be addressed to Yoshiyuki Henning.

Reprints and permission information is available at http://www.nature.com/reprints

Publisher's note Springer Nature remains neutral with regard to jurisdictional claims in published maps and institutional affiliations.